# Spin-orbital mixing in the topological ladder of the two-dimensional metal PtTe<sub>2</sub>

M. Qahosh , M. Masilamani , H. Boban, Xiao Hou, G. Bihlmayer , Y. Mokrousov , W. Karain, J. Minár , F. Reinert , L. Schusser , S. C. M. Schneider , 16,7 and L. Plucinski , Reinert Let Grünberg Institut (PGI-6), Forschungszentrum Jülich GmbH, 52428 Jülich, Germany Experimentelle Physik VII and Würzburg-Dresden Cluster of Excellence ct.qmat, Universität Würzburg, Würzburg, Germany Peter Grünberg Institut (PGI-1), Forschungszentrum Jülich and JARA, 52428 Jülich, Germany Department of Physics, Birzeit University, P.O. Box 14, Birzeit, Palestine Sew Technologies-Research Center, University of West Bohemia, 30614 Pilsen, Czech Republic Fakultät für Physik, Universität Duisburg-Essen, 47048 Duisburg, Germany Physics Department, University of California, Davis, California 95616, USA

(Received 7 February 2025; revised 30 June 2025; accepted 9 September 2025; published 14 October 2025)

We visualize the topological ladder and band inversions in PtTe<sub>2</sub> using spin-polarized photoemission spectroscopy augmented by three-dimensional momentum imaging. This approach enables the detection of spin polarization in dispersive bands and provides access to topological properties beyond the reach of conventional methods. Extensive mapping of spin-momentum space reveals distinct topological surface states, including a surface Dirac cone at a binding energy  $E_B \sim 2.3 \, \text{eV}$  and additional states at  $E_B \sim 1.6 \, \text{eV}$ ,  $E_B \sim 1.0 \, \text{eV}$ , and near the Fermi level. The electronic structure analysis demonstrates strong hybridization between Pt and Te atomic orbitals, confirming the nontrivial topology of these surface states. Furthermore, by comparison to one-step model photoemission calculations, we identify a robust correlation between the initial-state and measured spin polarizations while revealing asymmetries in specific experimental spin textures. These asymmetries, absent in the initial states due to symmetry constraints, arise from the breaking of time-reversal symmetry during the photoemission process, emphasizing the crucial influence of symmetries on experimental signatures of topology. A phase analysis of ladder states in real space suggests a route to probe them using photoemission, paving the way towards spectroscopic access to the quantum geometric tensor.

## DOI: 10.1103/vcgr-qjyy

## I. INTRODUCTION

1T transition-metal dichalcogenides (TMDCs) form a class of materials that exhibit numerous important electronic phenomena, including correlated and topological phases [1–6]. In particular, Pd and Pt selenides and tellurides exhibit a so-called topological ladder stemming from a series of band inversions in the chalcogen-derived p-band manifold [3] with several resulting spin-polarized topological states [1]. The determination of the topological properties of these materials requires probing spin-momentum dependence over the full Brillouin zone in order to access the Bloch wave functions, including their spin and orbital characters, as well as phases, that enter the quantum geometric tensor [7,8]. Angle-resolved photoemission spectroscopy (ARPES) is the most powerful technique for experimental electronic band-structure determination

Published by the American Physical Society under the terms of the Creative Commons Attribution 4.0 International license. Further distribution of this work must maintain attribution to the author(s) and the published article's title, journal citation, and DOI.

[9], and can access, albeit indirectly [10], spin band characters through its spin-polarized (SARPES) variant.

Compounds containing heavy elements typically exhibit spin-polarized surface states that exist in the local gaps of the projected band structure and emerge through band inversion at time-reversal invariant momenta (TRIM) points, therefore have the same origin as topological ones [11]. The topological ladder of highly spin-polarized spin-momentum-locked states in PtTe<sub>2</sub> stems from several such band inversions [1,3], with additional effects due to hidden spin polarization [12,13] also present. We demonstrate how the interatomic interference effects due to strong orbital intermixing [14], augmented with spin-orbit scattering, lead to complex photoemission spin textures that reflect surface symmetries and carry rich information on the amplitude and phases of initial wave functions. Our findings underscore the utility of SARPES momentum maps for visualizing the topological ladder in TMDCs and exploring the topological properties of quantum materials more broadly.

### II. RESULTS

The surface of  $1T - \text{PtTe}_2$  exhibits three mirror planes which are oriented along the  $\overline{\Gamma M}$  reciprocal directions.

<sup>\*</sup>Contact author: l.plucinski@fz-juelich.de

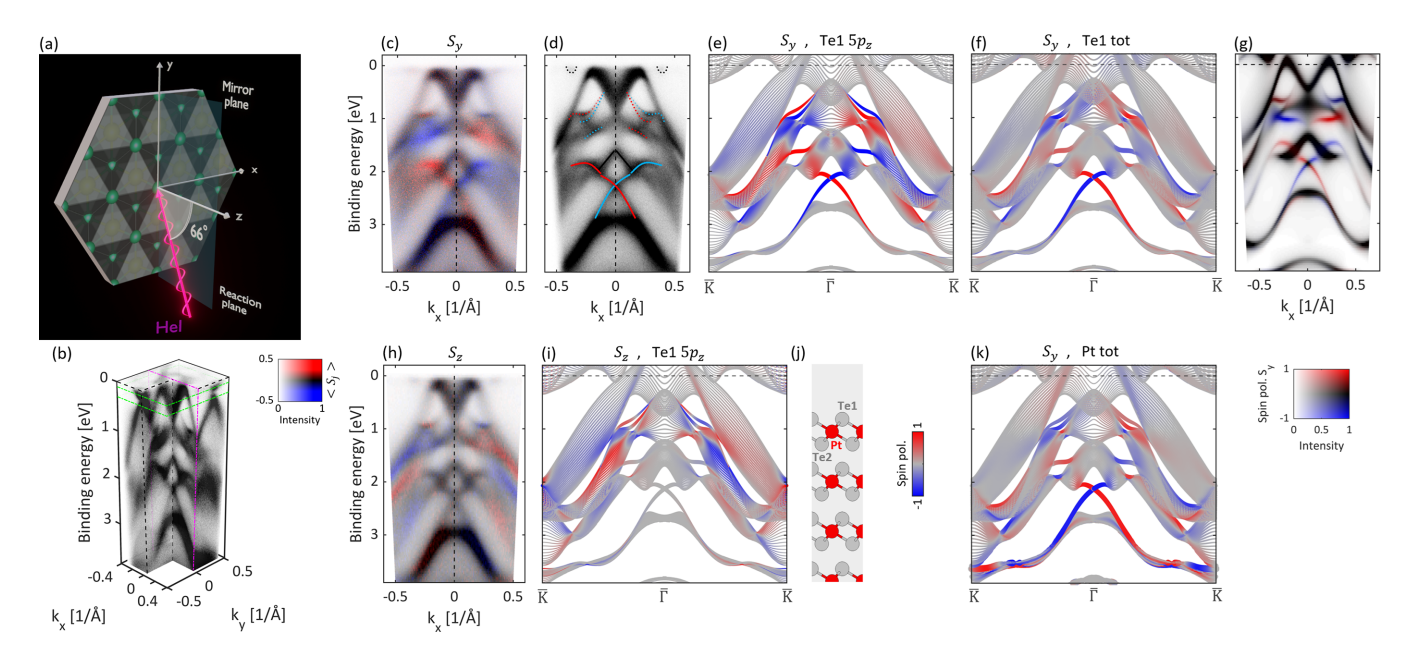


FIG. 1. (a) Experimental geometry where the reaction plane coincides with the  $\mathcal{M}_x$  mirror plane of the sample's surface. (b) Spin-integrated experimental three-dimensional (3D) data. (c) Spin-polarized map for the cut indicated by the magenta frame in (b), where color indicates  $S_y$ . (d) Identification of topological ladder features present in (c) on top of a spin-integrated map. (e) Related *ab initio* spin-polarized surface electronic structure calculation, where the line thickness indicates the weight and the color the spin expectation value  $S_y$  for surface Te  $5p_z$  orbitals. (f) Same as (e) but for the total weight on the surface Te atom. (g) Simulation of (c) calculated using the SPR-KKR [15] packet. (h) Same as (c) but for  $S_z$ . (i) Same as (e) but for  $S_z$ . (j) Schematic indication of the surface Te 1 atom, the outermost Pt atom, and the third layer Te2 atom. (k) Same as (f) but for the Pt atom.

Figures 1(a)-1(g) show SARPES maps and ab initio calculations for the experimental geometry depicted in Fig. 1(a), where one of the sample mirror planes,  $\mathcal{M}_x$ , is preserved. Figure 1(b) shows the experimental spin-integrated band structure, with the magenta frame depicting the plane in which the SARPES map in Fig. 1(c) for the spin expectation value  $S_{\nu}$  [refer to the coordinate system definition in Fig. 1(a)] has been measured. Since  $S_v$  is parallel to  $\mathcal{M}_x$ , through the axial vector mirror reflection rules, the map in Fig. 1(c) must obey  $S_v(k_x, k_v, E) = -S_v(-k_x, k_v, E)$ , which it indeed does. Figure 1(c) exhibits several spin-polarized states related to the topological ladder, which for clarity are depicted by solid lines in Fig. 1(d) on top of the spin-integrated map. Additional dashed lines depict surface resonances and other pronounced features. All of these are reproduced in the *ab initio* calculation in Fig. 1(e), where the false color map and the thickness of the lines refer to spin polarization and partial charge of the  $5p_z$  orbital of the surface Te atom. An additional calculation in Fig. 1(f) shows the total charge on surface Te atoms, where the comparison to the experiment is less favorable than in Fig. 1(e), especially in the region of ladder states at  $\approx 1 \text{ eV}$ . Figure 1(g) shows the SARPES spectrum related to Fig. 1(c) calculated with the spin-polarized relativistic Korringa-Kohn-Rostoker (SPR-KKR) package [15] using a free-electron final state and demonstrating excellent agreement for virtually all experimental features.

Figures 1(h) and 1(i) show similar experimental and theoretical results as Figs. 1(c) and 1(e) but for the out-of-plane spin expectation value  $S_z$ , where again a favorable agreement is found. For convenience, Fig. 1(j) schematically depicts the

outermost Te and Pt atoms from which the majority of the photoemission signal originates through the method's surface sensitivity, and Fig. 1(k) shows the theoretical  $S_y$  calculation for that Pt atom, indicating that the topological ladder wave functions are strongly mixed between the surface-most Pt and Te sites. Taking into account the photoionization cross sections [16,17], photoelectron mean free path, and expected angular distributions from atomic orbitals at the experimental incident angle of  $\theta_{hv}=66^\circ$ , the dominant photocurrent contributions for the topological ladder states are expected from both Te  $5p_z$  and Pt  $5d_{z^2}$  orbitals.

The Dirac cone states in Fig. 1(c) at  $E_B \approx 2.3 \,\mathrm{eV}$  are strongly spin polarized, which is consistently reproduced in Figs. 1(e), 1(f), 1(g), and 1(k), therefore their  $S_y$  polarization is robust. However, the difference between Te  $5p_z$  partial charges in Fig. 1(e) and total charge calculations in Figs. 1(f) and 1(k), in particular for the ladder states at  $\approx$ 1 eV, indicates their complex spin texture in real space.

The in-plane spin texture in PtTe<sub>2</sub> follows from a Rashbalike mechanism due to the out-of-plane potential gradient. On the other hand, the out-of-plane spin texture results from the intralayer in-plane dipoles, which exist along directions orthogonal to the mirror planes [13]. Despite the different origins of the two effects, the  $S_y$  and  $S_z$  spin polarizations in Figs. 1(c) and 1(h), respectively, appear to be similar, with the main difference being a small  $S_z$  polarization in the Dirac cone, theoretically reproduced in Fig. 1(i).

Figure 2 shows SARPES maps and *ab initio* calculations for the experimental geometry depicted in Fig. 2(a), where none of the sample mirror planes is preserved.

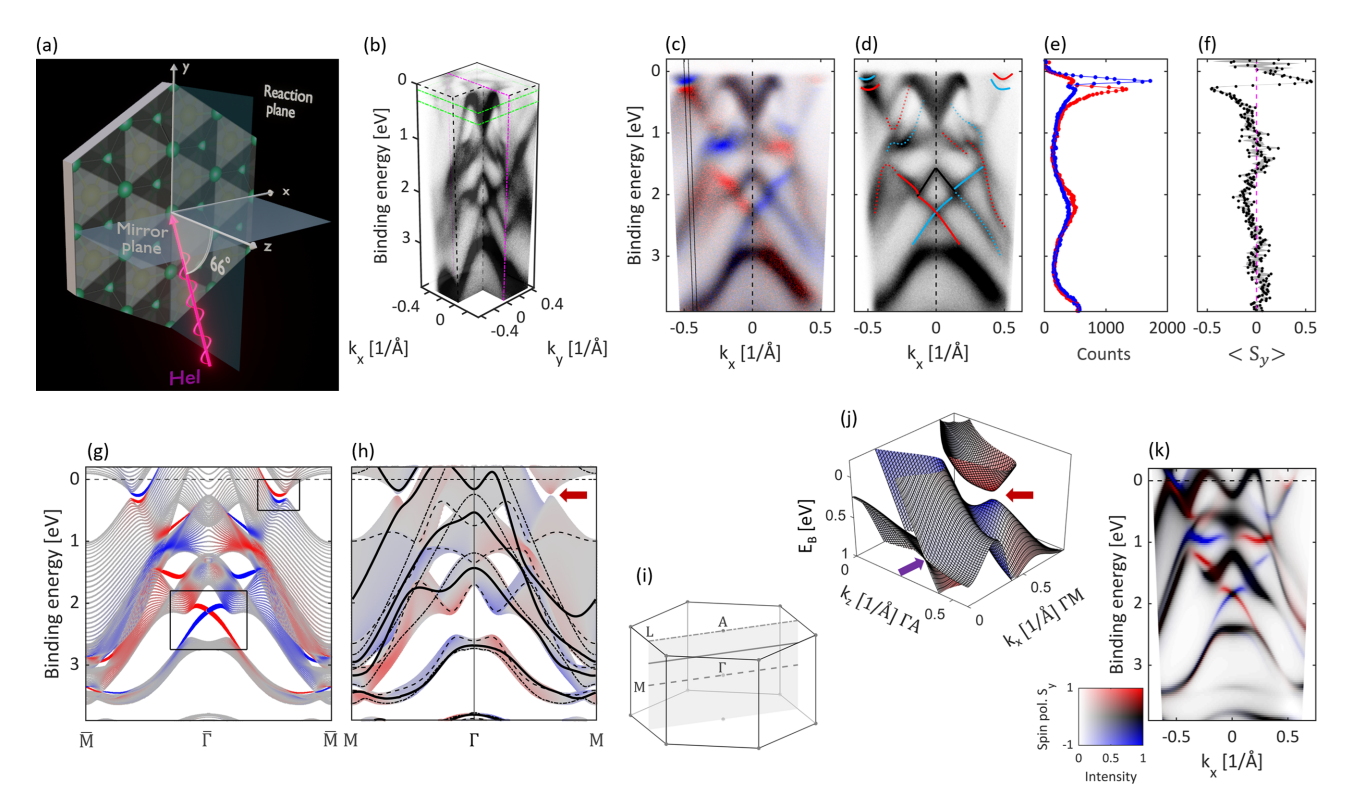


FIG. 2. (a) Experimental geometry where the reaction plane is orthogonal to the  $\mathcal{M}_y$  mirror plane of the sample's surface. (b) Spin-integrated experimental 3D data. (c) Spin-polarized map for the cut indicated by the magenta frame in (b), where color indicates  $S_y$ . (d) Identification of topological ladder features present in (c) on top of a spin-integrated map. (e) Spin-polarized EDCs for the region in (c) enclosed by the black lines. (f) Related spin polarization. (g) *Ab initio* spin-polarized surface electronic structure calculation where the line thickness indicates the weight and the color the spin expectation value  $S_y$  for surface Te  $S_{p_z}$  orbitals. (h) Related spin-polarized bulk projected band structure with the dashed lines showing bands along  $M\Gamma M$ , the dashed-dotted lines along LAL, and with the solid lines showing bands along a line that cuts through the middle of the  $\Gamma A$  line, as shown in (i). (j) Bulk band structure for  $E_B(k_x, k_z)$ . Dark red arrows in (h) and (j) indicate the local bulk band gap, while the purple arrow in (j) indicates the type-II bulk Dirac cone. (k) One-step photoemission model calculation related to the map (c).

Figure 2(b) shows an experimental spin-integrated band structure, with the magenta frame depicting the plane along which the SARPES map in Fig. 2(c) for the spin expectation value  $S_y$  [refer to the coordinate system definition in Fig. 2(a); compared to Fig. 1, the sample has been rotated] has been measured. The identified topological ladder states are depicted in Fig. 2(d), while Figs. 2(e) and 2(f) show the energy distribution curve (EDC) and spin polarization in the region between the two solid lines in Fig. 2(c) where the surface states near the Fermi level with  $S_y$  over 50% are located. States identified in Fig. 2(d) are in good overall agreement with the spin-polarized calculation for the surfacemost Te  $5p_z$  orbital shown in Fig. 2(g).

In Fig. 2(c), the  $S_y$  spin polarization is antisymmetric between  $S_y(E_B, k_x, k_y)$  and  $S_y(E_B, -k_x, k_y)$ . However, since the experimental setup of Fig. 2(a) does not have any mirror planes, no such rules relating  $S_y(E_B, k_x, k_y)$  with  $S_y(E_B, -k_x, k_y)$  exist for the experimental SARPES map, and the maps in Figs. 2(c) and 2(d) exhibit clear asymmetries, both regarding the spin polarization and the energy position of the dispersive features. For surface states this phenomenon, previously revealed for WTe<sub>2</sub> [14], is related to the interatomic interference and time-reversal symmetry breaking in the photoemission process, while for bulk states to the asymmetric

initial band-structure dispersions for generic values of  $k_z$  momenta, as shown in Figs. 2(h) and 2(i), through approximate  $k_z$  selectivity of ARPES [18]. Importantly, wave-function mixing between different sites is necessary to induce the effect for surface states, which provides an additional confirmation for such mixing in the PtTe<sub>2</sub> topological ladder. Figure 2(j) shows calculated  $E_B(k_x, k_z)$  bulk bands, highlighting the local band gap where the strongly spin-polarized state visualized in Fig. 2(e) is located, as well as the type-II bulk Dirac cone [19]. Figure 2(k) presents the SPR-KKR [15] calculation corresponding to the map in Fig. 2(c), incorporating the aforementioned effects and confirming the strong  $\pm k_x$  asymmetries observed in the experiment.

Figures 3(a)–3(i) show the experimental geometry and SARPES constant energy maps (CEMs) for two different binding energies [as indicated by green contours in Figs. 1(b) and 2(b)] and different sample rotations  $\phi$ , as defined in Fig. 3(a). The related calculated initial band structure maps are shown in Figs. 3(j) and 3(k). These maps aim at imaging strongly spin-polarized states near the Fermi level [see, e.g., Fig. 2(e)]. Indeed, in all maps one can see a spin-polarization sign inversion between  $E_B = 0.1$  and 0.3 eV, however, strong effects related to the incident light direction are observed. Due to the trigonal symmetry of PtTe<sub>2</sub>, when  $\phi$  is changed by 60°

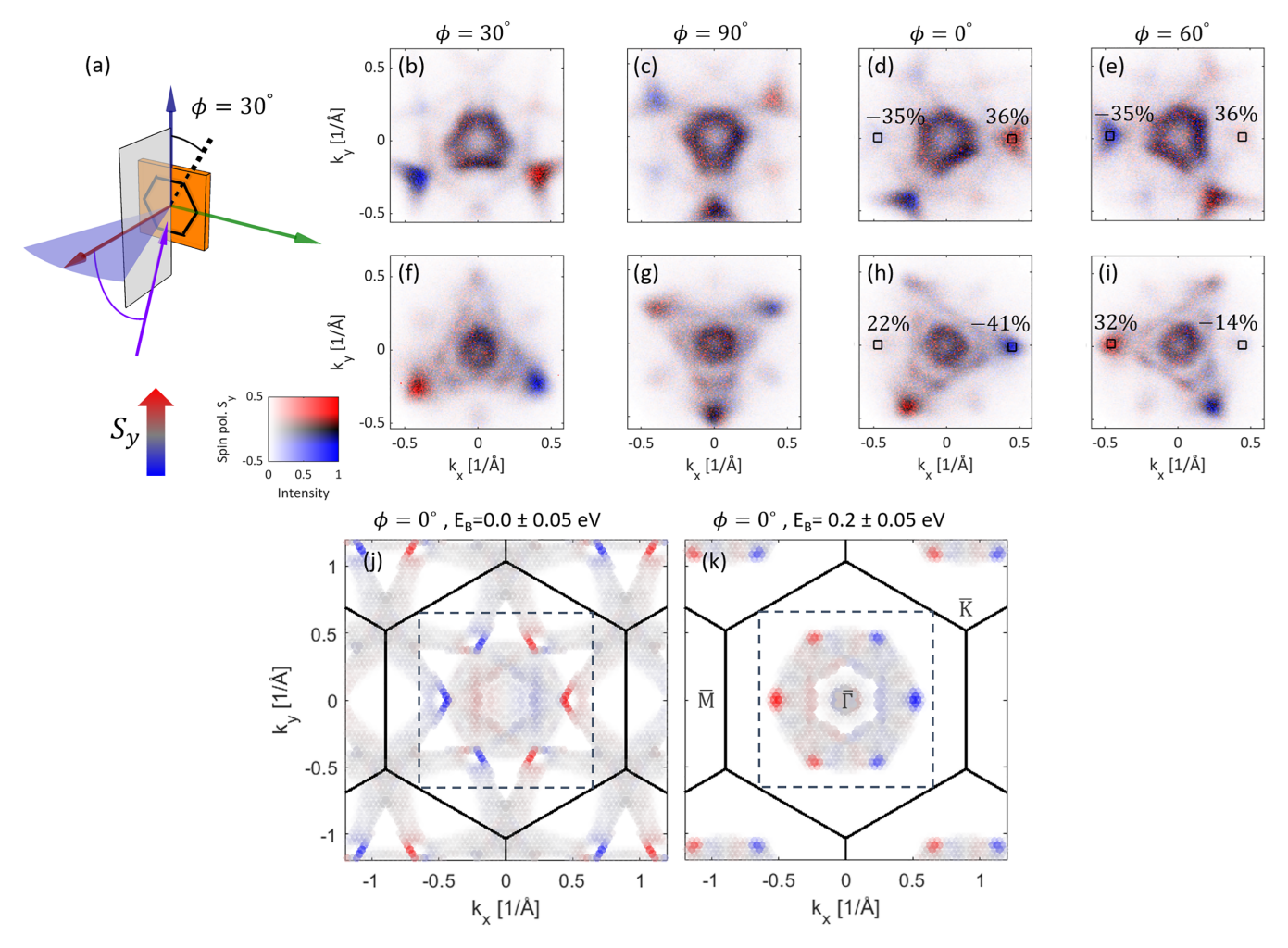


FIG. 3. (a) Experimental geometry indicating the rotation of the sample with respect to the z axis by an angle  $\phi$ . (b)–(e) Experimental SARPES maps for  $\phi = 30^{\circ}$ ,  $90^{\circ}$ ,  $0^{\circ}$ , and  $60^{\circ}$ , respectively, at a binding energy  $E_B = 0.1$  eV. (f)–(i) Same as (b)–(e) but at  $E_B = 0.3$  eV. (j), (k) Theoretical spin-polarized constant energy maps at  $E_B = \pm 0.05$  eV and  $E_B = 0.2 \pm 0.05$  eV, respectively.

the SARPES results are different. This makes the maps of Figs. 3(b) and 3(c), where the mirror plane coincides with the reaction plane, not only appearing rotated by  $\Delta \phi = 60^{\circ}$ but also exhibiting a different intensity pattern and a different strength of spin polarization [same for Figs. 3(f) and 3(g)]. For the geometry where the mirror plane is orthogonal to the reaction plane, the maps of Figs. 3(d) and 3(e) are expected to be related to each other by the  $\mathcal{M}_x$  transformation, which is indeed observed in experiment [same for Figs. 3(h) and 3(i)]. These asymmetric intensities do not influence the polarization for the lower binding energy states in Figs. 3(d) and 3(e), which are at 35%-36%. However, the measured polarizations are very different in Fig. 3(h) with a difference of 19% [similarly in Fig. 3(i)]. Since the initial surface states are nearly fully polarized, the most likely reason is the influence of the bulk projected states, which are influencing more the higher-energy states, as shown in Fig. 3(k).

Figure 4 provides a detailed breakdown of various components appearing in the SARPES process. Due to the short inelastic mean free path, the majority of the ARPES signal originates from the three outermost layers [20], depicted in Fig. 4(a) (further layers must be considered in quantitative

modeling). Due to the in-plane periodicity, it is sufficient to consider only the three atoms in the unit cell. Figure 4(b) depicts the interatomic interference process [14,21], which is sufficient to qualitatively explain the asymmetries of Fig. 2(c). However, even in a tight-binding picture, in a quantitative simulation one needs to consider a true spherical wave originating from every participating orbital, which means that multiple scattering, which includes spin-orbit coupling (SOC) scattering, needs to be considered. Pictorially this is indicated in Fig. 4(c), where a spherical wave, originating from one site, will be scattered by all the sites.

Figures 4(d) and 4(e) show real-space wave functions for the two representative topological ladder surface states, along the cut shown in Fig. 4(g) (further details are provided in the Supplemental Material [17]). In the case of the Dirac cone state in Fig. 4(d), one can visually recognize dominant Te1  $5p_z$  and Pt  $5d_{z^2}$  orbitals in the two outermost atomic layers, with the lower lobe of the Te  $5p_z$  being in phase with the outer lobes of Pt  $5d_{z^2}$ . A very different orbital character of Te1 and Te2 sites is evident. One can also see that the first and second PtTe<sub>2</sub> layers are approximately out of phase. The orbital composition of the state near the Fermi level [Fig. 4(e)]

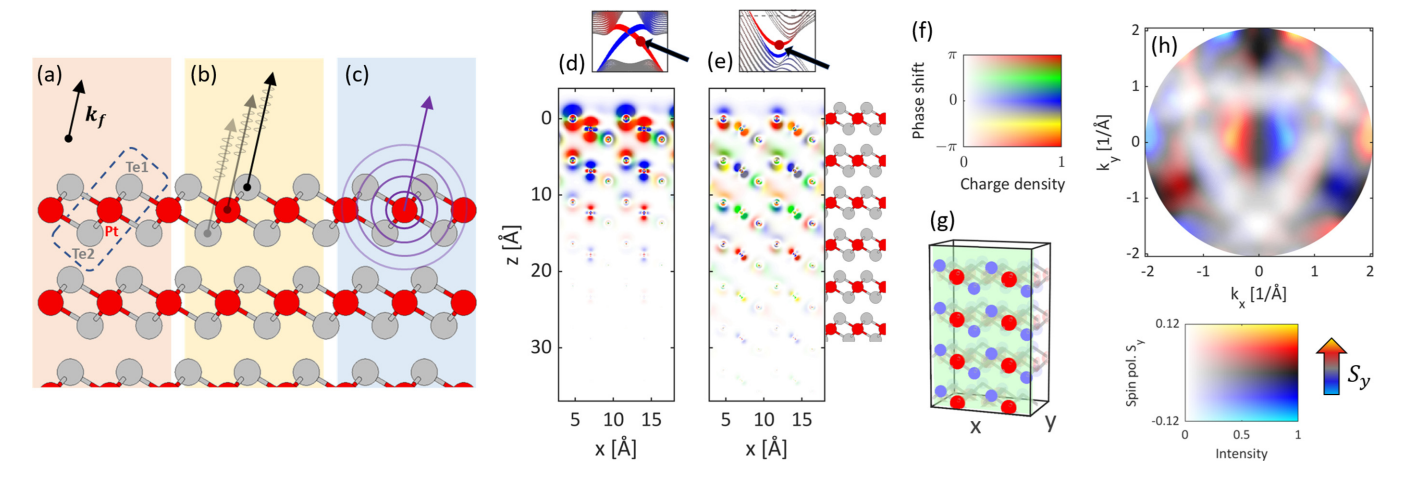


FIG. 4. (a) Indication of the 3 atoms in the unit cell of the outermost PtTe<sub>2</sub> layer. (b) The photoemission signal can be considered as a far-field coherent sum of electron waves originating from different atomic sites. (c) Spherical wave originating from the Pt site. (d) Real space wave function for one of the Dirac cone states. (e) Same as (d) but for one of the surface states near the Fermi level. (f) Two-dimensional colormap used to visualize both charge density and wave function phase in (d)–(e) [phase refers to the periodic part of the Bloch wave  $u(\mathbf{r})$ , the  $e^{i\mathbf{k}\cdot\mathbf{r}}$  factor is omitted]. (g) Visualization of the cut shown in (d)–(e). (h)  $S_y$  spin-polarization in the photoelectron diffraction pattern for SOC-scattering of the s-wave emission from the outermost Pt site in bulk PtTe<sub>2</sub> at  $E_{kin} = 16$  eV, with the related 2D colormap used.

is different, with the state being less localized, and with more charge in the interstitial regions between PtTe<sub>2</sub> layers.

Figure 4(h) provides insight into how much SOC scattering alone can influence SAPRES maps from PtTe<sub>2</sub>. We have performed a real-space atomic cluster calculation [22], where we have emitted an unpolarized electron *s* wave from the Pt atom, as depicted in Fig. 4(c). Since PtTe<sub>2</sub> is nonmagnetic (i.e. no exchange scattering), without SOC scattering such a wave would not lead to spin-polarized electrons, even if multiply scattered. However, with spin-orbit scattering, a spin polarization of up to 12% is present at certain emission angles. This value is likely smaller in actual SARPES maps, since the angular regions of high-spin polarization must coincide with emission angles where bands appear, and, furthermore, the coherent sum of emissions from different sites must be considered.

### III. DISCUSSION

We demonstrate that experimental spin textures of the topological ladder states in PtTe2 reveal contributing orbital characters through the excitation process. Strong asymmetries observed in Fig. 2(c) show that the details of the measured polarization results from the interdependence of several effects that include interatomic interference, the perpendicular momentum sensitivity of SARPES, as well as the SOC scattering processes. Some features due to these effects can be modeled using ab initio methods, as shown in Figs. 2(h) and 2(j) and in Figs. 4(d) and 4(e). Importantly, a favorable agreement to SPR-KKR calculations with the free-electron final-state model is obtained, which confirms that in PtTe<sub>2</sub>, SOC scattering, although not negligible [Fig. 4(h)], is not critical. Figure 3 demonstrates how details of experimental geometry influence measured spin polarizations and thus the necessity of measuring SARPES maps over large momentum regions.

The innovative way of visualizing the  $\psi_i$  of the topological ladder states in Figs. 4(d) and 4(e) provides an intuitive connection between surface topology and photoemission intensity. The phase structure of real-space wave functions is critical in the quantum geometric tensor, thus accessing it experimentally is one of the key challenges of solid state spectroscopies. In the matrix element  $\langle \psi_{\mathbf{k}_f} | \mathbf{A} \cdot \mathbf{p} | \psi_i \rangle$  one assumes the  $\psi_{\mathbf{k}_f}$  to be a time-reversed low-energy electron diffraction (LEED) state, which includes an evanescent  $\approx e^{i\mathbf{k}_f \cdot \mathbf{r}}$  component. At He I excitation one can assume  $E_{\rm kin} \approx 16\,{\rm eV}$  and an inner potential  $V_0 \approx 10 \, \text{eV}$ , with the wavelength of the normal emission photoelectron inside the solid of  $\approx$ 2.4 Å. The inner product of  $\psi_{\mathbf{k}_f}$  with the polarization-modulated gradient of  $\psi_i$  leads to hv-dependent intensity modulations that therefore can experimentally reveal the phase structure of  $\psi_{\mathbf{k}_f}$  (further details are provided in the Supplemental Material [17]).

In summary, we have demonstrated how the properties of topological ladder states are manifested in SARPES spectra. By addressing the challenges posed by intersite orbital mixing and SOC scattering, our work provides a foundation for the quantitative derivation of the quantum geometric tensor in solids using ARPES spectra.

### ACKNOWLEDGMENTS

L.P. would like to thank Frank Freimuth for fruitful discussions. M.Q. was supported by the Federal Ministry of Education and Research of Germany in the framework of the Palestinian-German Science Bridge (BMBF Grant No. 01DH16027). H.B. was supported by the DFG via the Project PL 712/5-1. X.H. was supported by Deutsche Forschungsgemeinschaft (DFG, German Research Foundation) under Germany's Excellence Strategy - Cluster of Excellence Matter and Light for Quantum Computing (ML4Q) EXC 2004/1 - 390534769. Y.M. acknowledges support by the EIC Pathfinder OPEN Grant No. 101129641 "OBELIX" and by the DFG - TRR 288 - 422213477 (Project B06). J.S. and

J.M. would like to thank the QM4ST project with Reg. No. CZ.02.01.01/00/22\_008/0004572, cofounded by the ERDF as part of the MŠMT.

#### DATA AVAILABILITY

The data that support the findings of this article is available from the authors upon reasonable request.

- [1] O. J. Clark, M. J. Neat, K. Okawa, L. Bawden, I. Marković, F. Mazzola, J. Feng, V. Sunko, J. M. Riley, W. Meevasana, J. Fujii, I. Vobornik, T. K. Kim, M. Hoesch, T. Sasagawa, P. Wahl, M. S. Bahramy, and P. D. C. King, Fermiology and superconductivity of topological surface states in PdTe<sub>2</sub>, Phys. Rev. Lett. 120, 156401 (2018).
- [2] Y. Li, Y. Xia, S. A. Ekahana, N. Kumar, J. Jiang, L. Yang, C. Chen, C. Liu, B. Yan, C. Felser, G. Li, Z. Liu, and Y. Chen, Topological origin of the type-II Dirac fermions in PtSe<sub>2</sub>, Phys. Rev. Mater. 1, 074202 (2017).
- [3] M. S. Bahramy, O. J. Clark, B.-J. Yang, J. Feng, L. Bawden, J. M. Riley, I. Marković, F. Mazzola, V. Sunko, D. Biswas, S. P. Cooil, M. Jorge, J. W. Wells, M. Leandersson, T. Balasubramanian, J. Fujii, I. Vobornik, J. E. Rault, T. K. Kim, M. Hoesch *et al.*, Ubiquitous formation of bulk Dirac cones and topological surface states from a single orbital manifold in transition-metal dichalcogenides, Nat. Mater. 17, 21 (2018).
- [4] C. W. Nicholson, M. Rumo, A. Pulkkinen, G. Kremer, B. Salzmann, M.-L. Mottas, B. Hildebrand, T. Jaouen, T. K. Kim, S. Mukherjee, K. Ma, M. Muntwiler, F. O. von Rohr, C. Cacho, and C. Monney, Uniaxial strain-induced phase transition in the 2D topological semimetal IrTe<sub>2</sub>, Commun. Mater. 2, 25 (2021).
- [5] B. Ghosh, D. Mondal, C.-N. Kuo, C. S. Lue, J. Nayak, J. Fujii, I. Vobornik, A. Politano, and A. Agarwal, Observation of bulk states and spin-polarized topological surface states in transition metal dichalcogenide Dirac semimetal candidate NiTe<sub>2</sub>, Phys. Rev. B 100, 195134 (2019).
- [6] S. Mukherjee, S. W. Jung, S. F. Weber, C. Xu, D. Qian, X. Xu, P. K. Biswas, T. K. Kim, L. C. Chapon, M. D. Watson, J. B. Neaton, and C. Cacho, Fermi-crossing type-II Dirac fermions and topological surface states in NiTe<sub>2</sub>, Sci. Rep. 10, 12957 (2020).
- [7] A. Gianfrate, O. Bleu, L. Dominici, V. Ardizzone, M. De Giorgi, D. Ballarini, G. Lerario, K. W. West, L. N. Pfeiffer, D. D. Solnyshkov, D. Sanvitto, and G. Malpuech, Measurement of the quantum geometric tensor and of the anomalous Hall drift, Nature (London) 578, 381 (2020).
- [8] M. Kang, S. Kim, Y. Qian, P. M. Neves, L. Ye, J. Jung, D. Puntel, F. Mazzola, S. Fang, C. Jozwiak, A. Bostwick, E. Rotenberg, J. Fuji, I. Vobornik, J.-H. Park, J. G. Checkelsky, B.-J. Yang, and R. Comin, Measurements of the quantum geometric tensor in solids, Nat. Phys. 21, 110 (2025).
- [9] J. A. Sobota, Y. He, and Z.-X. Shen, Angle-resolved photoemission studies of quantum materials, Rev. Mod. Phys. 93, 025006 (2021).
- [10] J. Henk, K. Miyamoto, and M. Donath, Retrieving the initial-state spin polarization from spin-resolved photoemission: Proposal for a case study on W(110), Phys. Rev. B 98, 045124 (2018).
- [11] B. Yan, B. Stadtmüller, N. Haag, S. Jakobs, J. Seidel, D. Jungkenn, S. Mathias, M. Cinchetti, M. Aeschlimann, and C.

- Felser, Topological states on the gold surface, Nat. Commun. 6, 10167 (2015).
- [12] X. Zhang, Q. Liu, J.-W. Luo, A. J. Freeman, and A. Zunger, Hidden spin polarization in inversion-symmetric bulk crystals, Nat. Phys. 10, 387 (2014).
- [13] O. J. Clark, O. Dowinton, M. S. Bahramy, and J. Sánchez-Barriga, Hidden spin-orbital texture at the Γ-located valence band maximum of a transition metal dichalcogenide semiconductor, Nat. Commun. 13, 4147 (2022).
- [14] T. Heider, G. Bihlmayer, J. Schusser, F. Reinert, J. Minár, S. Blügel, C. M. Schneider, and L. Plucinski, Geometry-induced spin filtering in photoemission maps from WTe<sub>2</sub> surface states, Phys. Rev. Lett. 130, 146401 (2023).
- [15] H. Ebert, D. Ködderitzsch, and J. Minár, Calculating condensed matter properties using the KKR-Green's function method recent developments and applications, Rep. Prog. Phys. 74, 096501 (2011).
- [16] J. Yeh and I. Lindau, Atomic subshell photoionization cross sections and asymmetry parameters:  $1 \le Z \le 103$ , At. Data Nucl. Data Tables **32**, 1 (1985).
- [17] See Supplemental Material at http://link.aps.org/supplemental/ 10.1103/vcgr-qjyy for the details of experimental and theoretical methods, which includes Refs. [23–35].
- [18] V. N. Strocov, L. L. Lev, F. Alarab, P. Constantinou, X. Wang, T. Schmitt, T. J. Z. Stock, L. Nicolaï, J. Očenášek, and J. Minár, High-energy photoemission final states beyond the free-electron approximation, Nat. Commun. 14, 4827 (2023).
- [19] M. Yan, H. Huang, K. Zhang, E. Wang, W. Yao, K. Deng, G. Wan, H. Zhang, M. Arita, H. Yang, Z. Sun, H. Yao, Y. Wu, S. Fan, W. Duan, and S. Zhou, Lorentz-violating type-II Dirac fermions in transition metal dichalcogenide PtTe<sub>2</sub>, Nat. Commun. 8, 257 (2017).
- [20] S. Beaulieu, J. Schusser, S. Dong, M. Schüler, T. Pincelli, M. Dendzik, J. Maklar, A. Neef, H. Ebert, K. Hricovini, M. Wolf, J. Braun, L. Rettig, J. Minár, and R. Ernstorfer, Revealing hidden orbital pseudospin texture with time-reversal dichroism in photoelectron angular distributions, Phys. Rev. Lett. 125, 216404 (2020).
- [21] P. Krüger, Photoelectron diffraction from valence states of oriented molecules, J. Phys. Soc. Jpn. 87, 061007 (2018).
- [22] F. J. García de Abajo, M. A. Van Hove, and C. S. Fadley, Multiple scattering of electrons in solids and molecules: A cluster-model approach, Phys. Rev. B 63, 075404 (2001).
- [23] M. Escher, N. B. Weber, M. Merkel, L. Plucinski, and C. M. Schneider, Ferrum: A new highly efficient spin detector for electron spectroscopy, e-J. Surf. Sci. Nanotechnol. 9, 340 (2011).
- [24] D. Wortmann, G. Michalicek, N. Baadji, M. Betzinger, G. Bihlmayer, J. Bröder, T. Burnus, J. Enkovaara, F. Freimuth, C. Friedrich, C.-R. Gerhorst, S. Granberg Cauchi, U. Grytsiuk, A. Hanke, J.-P. Hanke, M. Heide, S. Heinze, R. Hilgers,

- H. Janssen, D. A. Klüppelberg *et al.*, FLEUR, Zenodo (2023), doi:https://doi.org/10.5281/zenodo.7576163.
- [25] P. Blaha, K. Schwarz, F. Tran, R. Laskowski, G. K. H. Madsen, and L. D. Marks, WIEN2k: An APW+lo program for calculating the properties of solids, J. Chem. Phys. 152, 074101 (2020).
- [26] H. Krakauer, M. Posternak, and A. J. Freeman, Linearized augmented plane-wave method for the electronic band structure of thin films, Phys. Rev. B 19, 1706 (1979).
- [27] J. P. Perdew, K. Burke, and M. Ernzerhof, Generalized gradient approximation made simple, Phys. Rev. Lett. 77, 3865 (1996).
- [28] J. Kessler, *Polarized Electrons* (Springer, Berlin, 1985).
- [29] F. Salvat, A. Jablonski, and C. J. Powell, ELSEPA—Dirac partialwave calculation of elastic scattering of electrons and positrons by atoms, positive ions and molecules (new version announcement), Comput. Phys. Commun. 261, 107704 (2021).
- [30] J. Pendry, Theory of photoemission, Surf. Sci. 57, 679 (1976).

- [31] J. Braun, The theory of angle-resolved ultraviolet photoemission and its applications to ordered materials, Rep. Prog. Phys. **59**, 1267 (1996).
- [32] J. Braun, J. Minár, and H. Ebert, Correlation, temperature and disorder: Recent developments in the one-step description of angle-resolved photoemission, Phys. Rep. 740, 1 (2018).
- [33] G. Malmström and J. Rundgren, A program for calculation of the reflection and transmission of electrons through a surface potential barrier, Comput. Phys. Commun. 19, 263 (1980).
- [34] M. Masilamani, J. Schusser, M. Qahosh, L. Plucinski, and F. Reinert, One-step model photoemission calculations of type-II Dirac semimetal PtTe<sub>2</sub>, AIP Conf. Proc. 3054, 070004 (2024).
- [35] P. J. Feibelman and D. E. Eastman, Photoemission spectroscopy—correspondence between quantum theory and experimental phenomenology, Phys. Rev. B 10, 4932 (1974).